Structure and dynamics of fluorescently labeled complex fluids by Fourier imaging correlation spectroscopy

Tyler J. Grassman, Michelle K. Knowles, and Andrew H. Marcus*

Materials Science Institute and Department of Chemistry, University of Oregon, Eugene, Oregon 97403

(Received 10 July 2000)

We present a method of Fourier imaging correlation spectroscopy (FICS) that performs phase-sensitive measurements of modulated optical signals from fluorescently labeled complex fluids. FICS experiments probe the time-dependent trajectory of a spatial Fourier component of the fluid particle density at a specified wave number k, and provide a direct route to the intermediate scattering function. The FICS approach overcomes signal sensitivity problems associated with dynamic light scattering, while offering a means to acquire time-dependent information about spatial distributions of fluorescent particles, superior in efficiency to direct imaging methods. We describe the instrumental setup necessary to perform FICS experiments, and outline the theory that establishes the connection between FICS observables and statistical mechanical quantities describing liquid state dynamics. Test measurements on monolayer suspensions of rhodamine labeled polystyrene spheres are detailed.

PACS number(s): 82.70.Dd, 87.64.−t, 87.15.Ya, 87.16.−b

I. INTRODUCTION

The dynamics of complex fluids is an area of fundamental importance and technological relevance. Macromolecular or mesoscopic translational motion is important in many different kinds of soft-matter systems ranging from self-organized block-copolymer films to protein transport through the interior of live biological cells. Traditionally, experimental information about the structure of polymer, colloid, and biomembrane materials is obtained by light scattering from ordered arrangements of atoms, molecules, or larger scattering centers [1]. The dynamics of these systems is studied by performing dynamic light scattering (DLS) measurements of the fluctuations of the scattered light intensity [2,3]. Such experiments reveal the existence of multiexponential relaxations that arise from complex interactions between fluid components occurring over a range of spatial and temporal scales [4]. Nevertheless, the dynamics of many intriguing soft materials have been left unexplored due to a lack of sufficient light scattering contrast.

Investigations of complex fluids are also constrained by the fact that many systems appear naturally (and commercially) in the form of membranes or thin films. The properties of thin-film materials are often dramatically different from those of the bulk, and these changes are thought to occur as a consequence of subtle differences in the underlying microscopic dynamics [5]. Because the volumes associated with thin-film materials are extremely small, experimental methods for characterizing mesoscopic translational motion require a high degree of signal sensitivity. The most sensitive techniques are based on measurements of fluorescently labeled substituents in which emission signals are detected against a dark background. Fluorescence methods have undergone a resurgence in recent years, as a consequence of technological innovations in optical imaging and detection methodology. State-of-the-art imaging equipment is capable of visualizing spatial chromophore distributions from ultralow fluorescence signals, in some cases from a single isolated molecule [6]. Direct visualization methods offer additional advantages over conventional fluorescence spectroscopies in that it is possible to measure *distributions* of physical quantities (such as particle positions) rather than just their mean values. In light of these breakthroughs, the application of single-molecule microscopy to complex fluid dynamics might seem readily attainable. However, because chromophore photobleaching prevents the recording of long particle trajectories, very few experiments have been accomplished that actually directly visualize the relatively large spatial and temporal scales necessary to study complex fluid dynamics.

Here we present an approach to the measurement of time-dependent spatial distributions of chromophore-labeled complex fluids, Fourier imaging correlation spectroscopy (FICS). FICS retains the wave number selectivity of DLS while overcoming its sensitivity problems by performing measurements of modulated fluorescence signals from the intersection of an interference excitation fringe pattern with a heterogeneous distribution of chromophores. Conventional fluorescence correlation spectroscopy (FCS), developed almost 30 years ago by Magde, Elson, and Webb [7], was originally recognized for its sensitivity based on changes in optical absorption coefficients and fluorescence quantum yields. Since that time FCS has been successfully used to study translational diffusion, chemical kinetic rate constants, rotational diffusion coefficients, flow rates, molecular weights, and molecular aggregation [8]. All of the above mentioned FCS experiments require a model dependent interpretation, which is based on the assumption that density fluctuations occur by diffusion. The wave number selectivity of FICS eliminates the model dependence from the analysis of density fluctuations detected in these measurements.

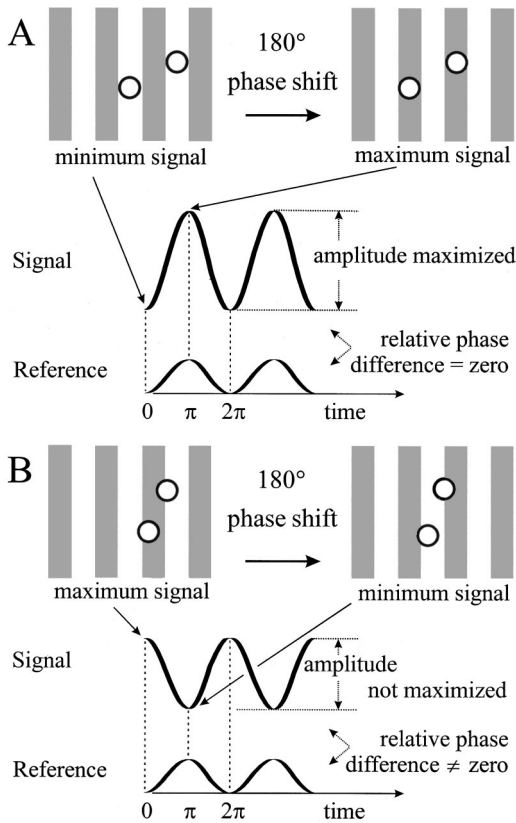*Author to whom correspondence should be sent. Email address: ahmarcus@fafnir.uoregon.edu

FIG. 1. Illustration of the basic principle underlying the FICS method. Two fluorescently labeled particles are exposed to an infinite periodic excitation grating with interfringe spacing d_G. Dark fringes correspond to regions of the grating where the optically generated excitation field is maximized. (A) For the particle configuration shown, the fluorescence intensity emitted from the particles varies with grating position as indicated. The modulated signal has a maximal amplitude, and oscillates in phase with the grating position. (B) A particle ''fluctuation'' results in a decrease in the signal modulation amplitude, and a finite phase shift relative to that of the grating position.

The basic FICS principle is illustrated for the simple case of a two-particle system in Fig. 1. Figure 1(A) shows a schematic diagram of two uniformly labeled fluorescent particles (with diameter σ) exposed to an infinite periodic excitation grating that is directed along the x axis. For the particle configuration shown, the x component of the interparticle separation, Δr_x, exactly matches the period of the grating, d_G. If the dark fringes correspond to the regions of the grating where the photon flux is greatest, the grating position shown on the left side of Fig. 1(A) will result in the least possible number of chromophores being optically excited. The average fluorescence intensity emitted from the particles, for this grating position, will therefore be minimized. If the particles remain stationary while the position of the excitation grating is translated along the direction of the x axis by the distance $d_G/2$ (a 180° phase shift), a maximal number of chromophores will be exposed to the excitation field, and the resulting fluorescence intensity will be maximized. The variation of the fluorescence intensity of the system as a function of grating position is indicated schematically for two zero-to-2π cycles. The amplitude of the modulated fluorescence signal is maximized for this particle configuration

($\Delta r_x \sim d_G$), and its phase relative to that of the arbitrarily chosen position of the grating is zero. We now consider the effect on the modulated fluorescence signal after the occurrence of a particle fluctuation. In Fig. 1(B) we show the same initial grating position as described above; however, the particle positions have changed so that Δr_x has decreased to a value slightly larger than $d_G/2$. For the particle configuration and grating position shown on the left side of Fig. 1(B), the fluorescence signal is maximized relative to other grating positions. As in the previous case, translation of the grating leads to a modulation of the fluorescence signal. However, the amplitude of the modulation is now smaller than before, since there is no grating position that can simultaneously excite all of the chromophores on the two particles. Thus the particle fluctuation illustrated in Fig. 1 results in a discernable decrease in the modulation amplitude of the fluorescence signal, and an increase in its relative phase with respect to the grating position.

Based on the above example, we can assign the following physical meaning to the FICS observables (phase and amplitude), and make a generalization to the same measurement performed on an N-body system. The amplitude of the modulated signal reflects the extent to which an N-body system contains spatial periodicity (or wave number k) that matches the spatial frequency of the excitation grating ($k_G = 2\pi/d_G$). For the purpose of this work, we consider only isotropic fluid systems so that all orientations of the excitation grating (and hence, all directions of the wave vector, $\mathbf{k}_G$) yield equivalent information. The phase of the modulated signal reflects the relative position (or phase) of the spatial periodicity at wave number k_G contained by the particle configuration with respect to the reference position (or phase) of the excitation grating. We show below that measurements of the phase and amplitude performed as described above contain all of the information needed to fully characterize the spatial Fourier component of the particle configuration at the spatial frequency k_G defined by the excitation grating.

While direct visualization methods provide simultaneous information about all spatial scales, FICS measurements isolate fluctuations of an N-body system at a single wave number. Execution of independent measurements at successive k values provides the statistically relevant information to determine two-point spatial and temporal distribution functions of the fluid. Furthermore, the spatial information contained in the FICS observable (corresponding to a single value of k) is collected much more efficiently than it is possible to record information over the full spectrum of k using direct visualization techniques [9]. We show below that for a sample containing N chromophore labeled particles, the maximum number of discrete times that can be sequentially recorded using FICS is N times the maximum number of frames recorded using video microscopy. Thus the most efficient use of the available photons for time-dependent studies is to detect fixed-k fluctuations from a large sample and to bin the maximal number of recorded time increments into the desired temporal range. Depending on the choice of data acquisition device, the dynamic range accessed by FICS experiments can exceed $\sim 10^{-8} - 10^2$ sec.

Although the FICS experimental setup is similar to that employed by other methods used to study liquid state dy-

namics [10–12], the focus of past work has been to determine the bulk diffusion coefficient. To our knowledge, this paper is the first full report of a fluorescence observable that directly probes the time-dependent trajectory of a complex spatial Fourier component of the fluid particle density, $\hat{C}(k,t)$, and thereby provides a direct route to the information necessary to construct a comprehensive statistical description of the fluid dynamics. While real-space trajectories contain all of the dynamical information that characterizes the $6N$ degrees of freedom of an N-body system with no internal degrees of freedom, taken as a whole this information is overwhelmingly complex, and requires extensive analysis to establish a microscopic picture of the fluid's behavior [13]. A more directly informative (and physically meaningful) description of the dynamics is obtained by considering statistically averaged time-dependent distribution functions. In particular, the van Hove space-time correlation function $G(r,\tau)$ is the conditional probability that a particle can be found at position r at time τ, given that either the same or a different particle was previously at position $r=0$ at time $t=0$ [14]. It is a straightforward exercise, though numerically intensive, to calculate $G(r,\tau)$ from a complete set of particle trajectories. In addition to the advantage of greater dynamic range discussed above, the FICS method provides a direct route to this same distribution.

In this work, we study the dynamics of a model complex fluid system, Rhodamine-labeled 1-μm poly(styrene) colloidal particles confined to monolayer suspensions, using both digital video fluorescence microscopy (DVFM) and FICS. We demonstrate that FICS data provide a more direct route to the same statistically relevant information yielded by the DVFM data, although the former is more easily obtained. The FICS method holds promise as a new tool to study a wide range of problems where fluorescence signals are extremely low such as intracellular transport in live cells [15] and polymer dynamics in ultrathin films.

II. THEORY AND BACKGROUND INFORMATION

A. Microscopic trajectories and statistical distribution functions

Digital video microscopy (DVM) [16,17] is an established method that has been successfully used to study complex fluid dynamics. When used to image fluorescently labeled particles, DVFM has both advantages and disadvantages. The strength of DVFM is that it provides detailed microscopic dynamical information. The observable in a DVFM experiment is a complete set of two-dimensional N particle trajectories $\mathbf{r}_1(t)$, from which we construct the time-dependent microscopic density

$$C(\mathbf{r},t) = \sum_{i=1}^{N} \delta[\mathbf{r}-\mathbf{r}_i(t)]. \qquad (2.1)$$

In Eq. (2.1), the index i enumerates the N ''particle'' positions $\mathbf{r}_i(t)$ in the fluid at time t. The choice of definition for a particle depends on the nature of the complex fluid being studied. For example, the positions may account for the internal structure of a fluid of anisotropic objects, or it may simply identify their centers of mass. The minimum time

interval is determined by the experimental sampling time between consecutive configurations. The experimental procedure is to image a representative area of the N-particle sample onto the detector face of a high resolution charge coupled device (CCD) video camera. The CCD detector is a two-dimensional array of single-element detectors (or pixels). The CCD records the locations of each particle by registering a threshold number of incident photons ε on at least N separate pixels of the array. The data record of particle positions is then transferred to a storage device, which requires a finite dead time (typically on the order of tens of milliseconds), before the process is repeated. The main limitation of DVFM is that the trajectory is ended when the chromophores in the sample are degraded. If each particle absorbs and re-emits an average total of Ω photons before it is photobleached, the maximum number of frames collected by the CCD is $i_{CCD} \sim N\Omega/N\varepsilon = \Omega/\varepsilon$.

In FICS experiments, information is acquired at a fixed value of k using a single-element detector. In this case, the maximum number of time channels that can be sequentially recorded from an N particle sample is $i_{FICS} \sim N\Omega/\varepsilon = N \times i_{CCD}$. Of course, both FICS and DVFM measurements actually measure relatively small fluctuations of the total photocurrent signal. However, this consideration does not significantly affect our estimates of i_{CCD} and i_{FICS}.

To test the principles of FICS, we performed measurements on model systems consisting of monolayer suspensions of rhodamine labeled poly(styrene) spheres (particle diameter, $\sigma = 1$ μm) confined between the glass walls of a thin capillary cell. The rhodamine chromophores are resonantly excited at $\lambda_{ex} = 532$ nm, and their fluorescence is detected at $\lambda_{em} = 605$ nm. Figure 2(A) displays a digitized fluorescence image of a dense colloid suspension with reduced areal density, $\rho^* = N\sigma^2/A = 0.51$ ($N \approx 4160$ particles contained by a area $A \approx 7850$ μm^2). The x and y axes are orthogonal real-space coordinates. The process of transforming the information contained in a sequence of digitized images into the time-dependent density profile described by Eq. (2.1) is given by a prescription outlined by Crocker and Grier [16]. Figure 2(B) displays a particle trajectory consisting of 20 consecutive particle configurations with an interframe time step of 33 msec. The trajectory data indicates that structural relaxation of local particle environments occur on this time scale (0.66 sec). Furthermore, over a range of time scales (0.033 sec $< \tau <$ 16 sec), particles appear to be segregated into two populations; those oscillating within pseudohexagonally ordered local domains, and those ''hopping'' among adjacent sites within stringlike channels [18].

The spatial information contained in a single digitized image is equivalent to that contained by the Fourier transformation of the spatial particle density [Eq. (2.1)],

$$\hat{C}(\mathbf{k},t) = \int d^3r \, \exp(-i\mathbf{k}\cdot\mathbf{r})C(\mathbf{r},t), \qquad (2.2)$$

where $\hat{C}(\mathbf{k},t) = |\hat{C}| \exp[i\alpha]$ is a complex number. Figure 2(C) displays the Fourier transform of the image shown in Fig. 2(A) multiplied by its complex conjugate, where the x and y axes are orthogonal reciprocal-space coordinates (k_x and k_y), and the origin is placed at the center of the frame.
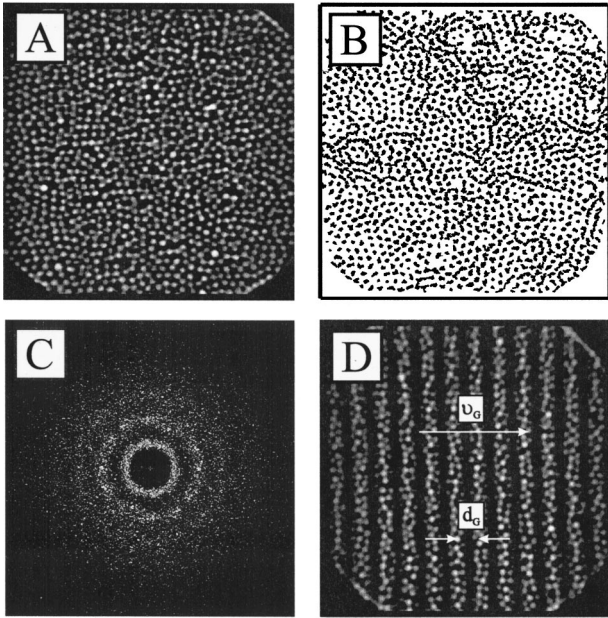
FIG. 2. (A) Fluorescence micrograph of a dense monolayer suspension of rhodamine labeled polystyrene spheres (diameter, σ = 1 μm, reduced areal density $\rho^* = N\sigma^2/A = 0.51$) that are optically excited by a uniform excitation profile. (B) Particle trajectory consisting of 20 consecutive configurations with an interframe time step of 33 msec. (C) Two-dimensional static structure function corresponding to the image shown in (A). (D) When the particles are excited by an interference fringe pattern ($d_G = 4.0 \ \mu$m), the resulting image is composed of a Fourier component with $k_G = 2\pi d_G^{-1}$, in addition to a band of low-k spatial components. In FICS experiments, the fringe pattern is swept across the sample with velocity v_G and angular frequency $\omega_G = k_G v_G (= 50 \text{ kHz})$.

This operation, averaged over all thermodynamically allowed particle configurations, defines the *static structure factor* [14]

$$S(\mathbf{k}) = \langle \hat{C}^*(\mathbf{k},t)\hat{C}(\mathbf{k},t) \rangle. \quad (2.3)$$

As mentioned previously, in this work we consider homogeneous isotropic fluids, so that the spatial correlation functions defined in this section depend only on the magnitudes $k = |\mathbf{k}|$ and $r = |\mathbf{r}|$, and not on the directions of $\mathbf{k}$ and $\mathbf{r}$. Thus $S(k)$ is independent of the orientation of $\mathbf{k}$, and a one-dimensional plot [averaged over the in-plane angle of Fig. 2(C)] is sufficient to describe its functional form. The structure exhibited by $S(k)$ is indicative of the important spatial frequencies that make up the image shown in Fig. 2(A). The first peak in $S(k)$ is most pronounced, and corresponds to a value of $k \sim 2\pi/\Delta r$, where Δr is the average spacing between neighboring particles in the fluid.

A statistical description of the fluid structure is given by the static pair distribution function, $g(r)$, which is the ensemble average probability of finding two particles separated by the distance r. It is obtained from $S(k)$ by Fourier transformation [14],

$$g(r) = \frac{1}{(2\pi)^3 \langle C \rangle} \int d^3k \exp(i\mathbf{k} \cdot \mathbf{r})[S(k) - 1], \quad (2.4)$$
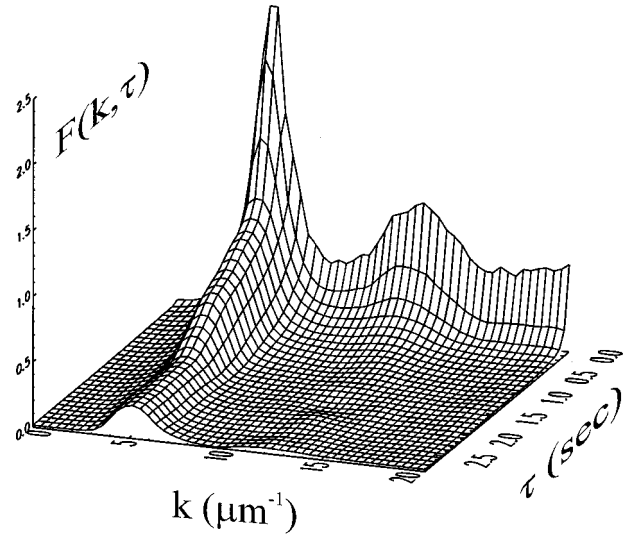

FIG. 3. The intermediate scattering function computed from DVFM trajectory data according to Eq. (2.5), and corresponding to the dense monolayer colloidal suspension shown in Fig. 2.

where $\langle C \rangle$ is the average fluid density. In principle, $g(r)$ can be obtained by numerically Fourier transforming experimental data provided a sufficiently wide range of k is sampled. From a practical standpoint, however, measurements of $S(k)$ are more often compared to the inverse Fourier transform of theoretical models of $g(r)$.

Dynamical information about the fluid is contained in time-dependent generalizations of $S(k)$ [14]. In particular, the intermediate scattering function is the two-point time-correlation function of the Fourier components, $\hat{C}(\mathbf{k},t)$,

$$F(k,\tau) = \langle \hat{C}^*(\mathbf{k},t)\hat{C}(\mathbf{k},t+\tau) \rangle, \quad (2.5)$$

where the zero-time limit $F(k,\tau=0) = S(k)$. Roughly speaking, the decay time of $F(k,\tau)$ at a particular value of k is given by $\tau_0 = [D_0 k^2]^{-1}$, which is the time required for an unhindered particle to diffuse (with diffusion coefficient D_0) the distance k^{-1}. Figure 3 displays the function $F(k,\tau)$, calculated from Fourier decomposition of particle trajectories according to Eq. (2.5), for the two-dimensional fluid previously described in Figs. 2(A), 2(B), and 2(C). Relaxations at the wave number k_{max} corresponding to the first peak in $S(k)$ have a complicated multiexponential form. Our observations of particle trajectories indicate that this multiexponential behavior results from the presence of spatially segregated processes. On the time scale of this measurement ($\sim$3 sec), there remains a residual correlation of structure at k_{max}, while no such structure persists at higher wave numbers.

The real-space dynamical distribution function, related to $F(k,\tau)$, is defined for an isotropic system by [14]

$$G(r,\tau) = \frac{1}{(2\pi)^3} \int d^3k \exp(i\mathbf{k} \cdot \mathbf{r})F(k,\tau)$$

$$= \langle C(r',t)C(r'+r,t+\tau) \rangle / \langle C \rangle. \quad (2.6)$$

The van Hove function $G(r,\tau)$ is the microscopic density-density time-correlation function previously described in
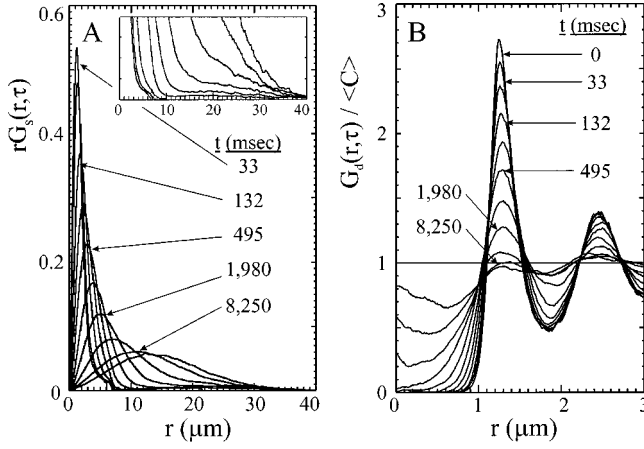
FIG. 4. The self-part and distinct part of the van Hove time-space correlation function [(A) and (B), respectively]. Both functions are computed from DVFM trajectory data corresponding to the dense monolayer colloidal suspension shown in Fig. 2. Both functions are computed according to Eq. (2.7). The inset in (A) shows the non-Gaussian tails in the self-displacement distribution functions that result from dynamic heterogeneity occurring on the indicated time and length scales.

Sec. I. The van Hove function separates into two terms, the ''self'' and ''distinct'' parts: $G(r,\tau) = G_S(r,\tau) + G_d(r,\tau)$, where

$$G_s(r,\tau) = \frac{1}{N}\left\langle \sum_{i=1}^{N} \delta[\mathbf{r} + \mathbf{r}_i(t) - \mathbf{r}_i(t+\tau)] \right\rangle,$$

(2.7)

$$G_d(r,\tau) = \frac{1}{N}\left\langle \sum_{i\neq j}^{N} \sum \delta[\mathbf{r} + \mathbf{r}_j(t) - \mathbf{r}_i(t+\tau)] \right\rangle,$$

with $G_S(r,0) = \delta(r)$ and $G_d(r,0) = \langle C \rangle g(r)$. In Figs. 4(A) and 4(B), we present calculations of the self-part and the distinct part of the van Hove function, according to Eq. (2.7), for the same dense colloidal fluid described in Figs. 2 and 3. The self-part, $G_S(r,\tau)$, is the time-dependent conditional probability density that a particle suffers a displacement $r = |\mathbf{r}(t) - \mathbf{r}(0)|$ during a time interval $t+\tau$. From our data we see that $G_S(r,\tau)$ is a single-mode Gaussian distribution for the shortest τ sampled (33 msec). For $0.033\,\text{sec} < \tau < 16\,\text{sec}$, the hopping processes observed in the particle trajectory lead to a non-Gaussian tail in $G_S(r,\tau)$ at large distances, until the distribution regains a Gaussian form for $\tau > 16\,\text{sec}$. On this long time scale, the fluid appears dynamically homogeneous. The distinct part $G_d(r,\tau)$ is the conditional probability density of finding a particle at time $t+\tau$ a distance r away from another particle at time t. The decay of $G_d(r,\tau)$ at the value of $r = r_{\text{max}}$ corresponding to the first peak of $g(r)$, describes the conditional probability of finding a pair of particles initially separated by the nearest-neighbor spacing at this same interparticle separation a time τ later. The data shown in Fig. 4(B) indicate that this quantity decays with a multiexponential form. For time increments longer than $\tau \sim 2\,\text{sec}$, the nearest-neighbor relaxation appears to plateau indicating a structural retardation on this length scale. Structural changes corresponding to the second (and

higher order) peaks of $g(r)$, however, are arrested on much shorter time scales ($0 < \tau < 132\,\text{msec}$).

The detailed real-space distribution functions displayed in Fig. 4 can, in principle, be obtained by Fourier inversion of the intermediate scattering function $F(k,\tau)$. Similarly to $G(r,\tau), F(k,\tau)$ separates into a self-part and a distinct part, each directly related to its real-space counterpart. $F_S(r,\tau)$ can be measured separately from $F(k,\tau)$ by performing experiments on ''tagged'' particles that are surrounded by a fluid of ''untagged,'' but otherwise identical, particles. We show below that $F(k,\tau)$ [and similarly, $F_S(k,\tau)$] can be measured quite accurately by performing separate time-dependent measurements as a function of k.

B. Fourier imaging correlation spectroscopy

In FICS experiments, the motion of chromophore labeled species is detected as slow fluctuations in fluorescence intensity from the intersection of an oscillatory excitation pattern (an optically generated grating) with a microscopically heterogeneous density of chromophores, $C(\mathbf{r},t)$. In the experiments reported here, the excitation pattern is created by the phase interference of two linearly polarized laser beams brought to a focus at the sample plane of a fluorescence microscope. The period of the fringe pattern, d_G, depends on the intersection angle φ between the two beams [19], and can be varied continuously from tens of microns to $\lambda_{\text{ex}}/2n$,

$$d_G = \frac{\lambda_{\text{ex}}}{2n\,\sin(\varphi/2)},$$

(2.8)

where n ($=1.38$; see Sec. III B below) is the relative refractive index of the dielectric interface upon which the beams are incident.

Figure 2(D) displays the resulting fluorescence image of the same dense colloidal suspension shown in Fig. 2(A) after it is illuminated by an excitation fringe pattern with $d_G = 4.0\,\mu\text{m}$. The size of the Gaussian envelope of the illuminated region is determined by the waist of the crossed laser beams at their focus, $w = 100\,\mu\text{m}$. At any instant in time, the oscillatory excitation profile picks out a small set of spatial Fourier components of the labeled particle distribution. There is a primary component at wave number $k_G = |\mathbf{k}_G| = 2\pi d_G^{-1}$, in addition to a $|\mathbf{k}| = 0$ component associated with the mean fluorescent light level, and a band of small-k contributions associated with the Gaussian envelope of the illuminated region. Temporal fluctuations in the integrated fluorescence intensity reflect the growth and decay of the spatial Fourier components represented by the image. Slow fluctuations of the chromophore distribution corresponding to the small-k spatial components arise from particles moving in and out of the illuminated sample region, and from slow drifts in the alignment of the laser spots. Other components of the signal include low frequency mechanical vibrations and detector electronic noise.

Fluctuations of the signal due solely to number density fluctuations at wave number k_G are selectively measured using the lock-in detection method [20]. A frequency generator is used to modulate the phase of the excitation fringe pattern from 0 to 2π at the angular frequency ω_G ($=50$ kHz). The pattern is thus swept across the illuminated sample region at
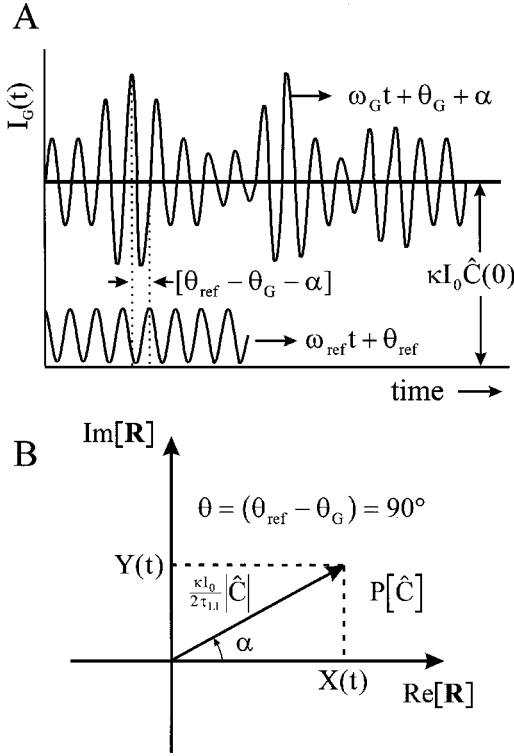
FIG. 5. (A) Schematic of the total fluorescence signal, $I_G(t)$, in relation to the reference waveform, $\cos(\omega_{ref}t + \theta_{ref})$. The modulated component $\kappa I_0|\hat{C}|\cos[\omega_G t + \theta_G + \alpha]$ oscillates in time at the angular frequency $\omega_G = k_G v_G$ with slowly varying amplitude $\kappa I_0|\hat{C}|$ and phase α. The mean background fluorescence level $\kappa I_0 \hat{C}(0)$ is time independent, as is the phase shift $\theta = \theta_{ref} - \theta_G$, which can be set to any arbitrary value. (B) The vector $\mathbf{R}(t) = X(t) + iY(t)$ fluctuates on the time scale of the particle motion, and follows a trajectory within the complex plane weighted by the probability distribution $P[\hat{C}]$. The geometric relationship between X, Y, α, and $|\hat{C}|$ is shown for the case $\theta = 90°$.

a velocity, $v_G(= \omega_G/k_G)$, greater than that with which a particle can travel the distance $2\pi k_G^{-1}$. The resulting integrated fluorescence intensity that emerges from the image is also modulated at the frequency ω_G. A schematic representation of the modulated fluorescence signal, relative to the phase of the excitation grating, is shown in Fig. 5(A). The illustration shows fluctuations of greatly exaggerated speed and amplitude. Because the continuous and periodic sweeping of the pattern by the distance d_G induces the signal modulation, this part of the signal is sensitive to density fluctuations on this same length scale. The lock-in detection method (explained below) determines the signal modulation at precisely the frequency ω_G, and ignores all signal contributions at other frequencies ($\omega \neq \omega_G$). Thus all components to the signal that are not correlated with the modulation frequency (including noise and density fluctuations corresponding to $k \neq k_G$) are excluded from the measurement.

The physical meaning of the modulated signal can be understood if we consider the total instantaneous fluorescence intensity $I_G(t)$, which is proportional to the spatial overlap of the oscillatory excitation profile, $I_{ex}(\mathbf{r})$, and the time-dependent density of labeled species, $C(\mathbf{r},t)$:

$$I_G(t) = \kappa \int C(\mathbf{r},t) I_{ex}(\mathbf{r}) d^3r = \frac{1}{(2\pi)^3} \kappa \int \hat{C}(\mathbf{k},t)\hat{I}_{ex}^*(\mathbf{k}) d^3k, \tag{2.9}$$

where $\hat{C}(\mathbf{k},t)$ is the Fourier transform of $C(\mathbf{r},t)$ given by Eq. (2.2), and κ is the proportionality factor that accounts for the absorption cross section, quantum yield, and light collection efficiency of the experimental system. The e^{-2} laser beam waist w is much larger than d_G. As a first approximation, the excitation profile can be represented by an infinite two-dimensional fringe pattern modulated in the direction of the x axis,

$$I_{ex}(\mathbf{x}) = I_0\{1 + \cos[\mathbf{k}_G \cdot \mathbf{x} + \phi(t)]\}, \tag{2.10}$$

where I_0 is a constant intensity. The time-dependent phase of the excitation grating, $\phi(t) = \omega_G t + \theta_G = \mathbf{k}_G \cdot v_G t + \theta_G$, completes a 0 to 2π cycle at the angular frequency ω_G, where the direction of $\mathbf{k}_G$ is parallel to v_G, and θ_G is a constant. The finite size of the actual beam reduces the number of fringes to $\sim \pi w/d_G$; however, a complete calculation for a fringe pattern having a Gaussian envelope [21], and showing the effect that a limited number of fringes has on our measurements, indicates that this does not qualitatively alter the meaning of $I_G(t)$ for $d_G \leq w/10$.

Substitution of the Euler formula into Eq. (2.10) followed by its Fourier transformation leads to

$$\hat{I}_{ex}(\mathbf{k}) = I_0[\delta(\mathbf{k}) + \tfrac{1}{2}\exp(i\phi)\delta(\mathbf{k} - \mathbf{k}_G)$$
$$+ \tfrac{1}{2}\exp(-i\phi)\delta(\mathbf{k} + \mathbf{k}_G)], \tag{2.11}$$

where δ is the Dirac delta function. Equation (2.11) shows that the excitation profile is composed of a stationary $k = 0$ contribution (the mean excitation light level), and modulated components corresponding to $\mathbf{k} = \pm\mathbf{k}_G$. Upon substitution of Eq. (2.11) into Eq. (2.9), we see that the modulated excitation profile picks out these same wave vector components from the chromophore density:

$$I_G(t) = \kappa I_0\{\hat{C}(0) + \tfrac{1}{2}[\exp[i\phi(t)]\hat{C}(\mathbf{k}_G,t)$$
$$+ \exp[-i\phi(t)]\hat{C}(-\mathbf{k}_G,t)]\}. \tag{2.12}$$

Because $C(\mathbf{r},t)$ is real, $\hat{C}(\mathbf{k}_G,t) = \hat{C}^*(-\mathbf{k}_G,t)$, and we write the fluorescence signal as

$$I_G(t) = \kappa I_0\{\hat{C}(0) + \tfrac{1}{2}[\exp[i\phi]\hat{C}(\mathbf{k}_G,t)$$
$$+ \exp[-i\phi]\hat{C}^*(\mathbf{k}_G,t)]\}$$
$$= \kappa I_0\{\hat{C}(0) + |\hat{C}|\cos[\phi + \alpha]\}, \tag{2.13}$$

where α is the phase angle associated with $\hat{C}$, namely $\alpha = \tan^{-1}[\text{Im }\hat{C}/\text{Re }\hat{C}]$. The schematic illustration [Fig. 5(A)] shows the signal, together with the reference oscillatory wave form used to generate the modulation: $\sin[\phi_{ref}(t)]$, where $\phi_{ref}(t) = \omega_{ref}t + \theta_{ref}$, and $\omega_{ref} = \omega_G$. The phase shift between the signal and reference wave forms is $\theta_{ref} - \theta_G + \alpha$. Equation (2.13) shows that the total signal is composed of a stationary (dc) and a modulated (ac) component. Because fluctuations of $\hat{C}(\mathbf{k}_G,t)$ occur at lower frequencies

than the modulation, the lock-in amplifier is used to demodulate the signal into slowly varying complex components, $X(t)$ and $Y(t)$, defined by the phase sensitive detection method [20]. This is accomplished by multiplying the signal [Eq. (2.13)] by the reference wave form, shifted by $0°[\sin(\phi_{ref})]$ and $90°[\cos(\phi_{ref})]$, respectively, and then employing a low-pass filter. This is operationally equivalent to performing the integrals

$$X(t) = \frac{1}{\tau_{L1}} \int_{-\infty}^{t} ds I_G(s) \sin[\phi_{ref}(s)] \exp[-(t-s)/\tau_{LI}],$$
(2.14)

$$Y(t) = \frac{1}{\tau_{LI}} \int_{-\infty}^{t} ds \, I_G(s) \cos[\phi_{ref}(s)] \exp[-(t-s)/\tau_{LI}],$$

where the lock-in time constant, τ_{LI}, and θ_{ref}, are experimentally adjustable, and s is the dummy variable of integration. Upon substitution of Eq. (2.13) into Eq. (2.14), we see that the integrands contain the products

$$|\hat{C}| \cos[\omega_G s + \theta_G + \alpha] \sin[\omega_{ref} s + \theta_{ref}],$$
(2.15)
$$|\hat{C}| \cos[\omega_G s + \theta_G + \alpha] \cos[\omega_{ref} s + \theta_{ref}],$$

for $X(t)$ and $Y(t)$, respectively. Using the trigonometric identities, we see that the integrands contain both oscillatory sum- and difference-frequency terms:

$$\frac{1}{2} |\hat{C}| \{ \sin[(\omega_G + \omega_{ref})s + \theta_G + \theta_{ref} + \alpha]$$
$$- \sin[(\omega_G - \omega_{ref})s + \theta_G - \theta_{ref} + \alpha] \},$$
(2.16)
$$\frac{1}{2} |\hat{C}| \{ \cos[(\omega_G + \omega_{ref})s + \theta_G + \theta_{ref} + \alpha]$$
$$+ \cos[(\omega_G - \omega_{ref})s + \theta_G - \theta_{ref} + \alpha] \},$$

for $X(t)$ and $Y(t)$, respectively. When τ_{LI} is set to a value much smaller than the timescale of the fluctuations of $\hat{C}(\mathbf{k}_G, t)$, the integration described by Eq. (2.14) has the effect of removing all of the time-varying components of the signal, while the stationary components remain. Since our reference and signal wave forms have the same frequencies ($\omega_G = \omega_{ref}$), the sum-frequency terms in Eq. (2.16) are removed and the difference frequency terms survive. Evaluation of Eq. (2.14) leads to

$$X(t) = \frac{\kappa I_0}{2 \tau_{LI}} \{ \text{Re}[\hat{C}] \sin \theta - \text{Im}[\hat{C}] \cos \theta \}$$

$$= \frac{\kappa I_0}{2 \tau_{LI}} |\hat{C}| \sin(\theta - \alpha),$$
(2.17)

$$Y(t) = \frac{\kappa I_0}{2 \tau_{LI}} \{ \text{Re}[\hat{C}] \cos \theta + \text{Im}[\hat{C}] \sin \theta \}$$

$$= \frac{\kappa I_0}{2 \tau_{LI}} |\hat{C}| \cos(\theta - \alpha),$$

where the phase shift $\theta = \theta_{ref} - \theta_G$ is the constant (and relatively short) time lag associated with the detection of fluorescence after it has been emitted from the sample. θ can be set to any arbitrary value by adjusting θ_{ref}.

Equation (2.17) shows that each X and Y is a function of the particle coordinates through its relationship to $\hat{C}(\mathbf{k}_G, t)$, and may therefore be considered a dynamical variable of the N particle system [14]. The real and imaginary parts of $\hat{C}(\mathbf{k}_G, t)$ can be isolated separately in X and Y, if θ is chosen to be an integer multiple of 90° or zero. Since the excited state lifetime of the rhodamine chromophores used in these studies are $\sim 10^{-9}$ sec, and the electronic delays are short, $\theta_G \approx 0$. Thus the phase shift can be arbitrarily adjusted such that $\theta = 90°$. Under these circumstances, $X(t) = \kappa I_0 \text{Re}[\hat{C}]/2\tau_{LI}$ and $Y(t) = \kappa I_0 \text{Im}[\hat{C}]/2\tau_{LI}$. Figure 5(B) shows a schematic representation of the complex components of the demodulated signal for the case $\theta = 90°$. Fluctuations of the vector $\mathbf{R}(t)[=X(t)+iY(t)]$ in the complex plane result as a direct consequence of the fluctuations of $\hat{C}(\mathbf{k}_G, t)$. The trajectory of $\mathbf{R}$ can be used to construct the probability distribution $P[\hat{C}]$, and therefore all of the time-correlation functions associated with $\hat{C}(\mathbf{k}_G, t)$.

The temporal and spatial two-point correlation functions of the complex fluid can be determined from measurements of $X(t)$ and $Y(t)$ without explicit knowledge of the phase angles θ and α. Using the definition of $F(k,\tau)$ [Eq. (2.5)] and $\hat{C}(\mathbf{k}_G, t) = \text{Re}[\hat{C}] + i\text{Im}[\hat{C}]$,

$$F(k,\tau) = \langle \text{Re}[\hat{C}(k,t)] \text{Re}[\hat{C}(k,t+\tau)] \rangle$$
$$+ \langle \text{Im}[\hat{C}(k,t)] \text{Im}[\hat{C}(k,t+\tau)] \rangle. \quad (2.18)$$

In Eq. (2.18), we have used the fact that the function $\hat{C}(k,t)$ has the property of even time-reversal symmetry [14]. The time-correlation function of the dynamical variable $X(t)$ [Eq. (2.17)] has the form

$$\langle X(t)X(t+\tau) \rangle = \frac{\kappa^2 I_0^2}{4 \tau_{LI}^2} \langle \{ \text{Re}[\hat{C}(k,t)] \text{Re}[\hat{C}(k,t+\tau)] \sin^2 \theta$$
$$+ \text{Im}[\hat{C}(k,t)] \text{Im}[\hat{C}(k,t+\tau)] \cos^2 \theta \} \rangle.$$
(2.19)

A similar expression describes the time-correlation function for the variable $Y(t)$:

$$\langle Y(t)Y(t+\tau) \rangle = \frac{\kappa^2 I_0^2}{4 \tau_{LI}^2} \langle \{ \text{Re}[\hat{C}(k,t)] \text{Re}[\hat{C}(k,t+\tau)] \cos^2 \theta$$
$$+ \text{Im}[\hat{C}(k,t)] \text{Im}[\hat{C}(k,t+\tau)] \sin^2 \theta \} \rangle.$$
(2.20)

Comparison of Eqs. (2.18), (2.19), and (2.20) shows that

$$F(k,\tau) = \frac{4 \tau_{LI}^2}{\kappa^2 I_0^2} \{ \langle X(t)X(t+\tau) \rangle + \langle Y(t)Y(t+\tau) \rangle \}.$$
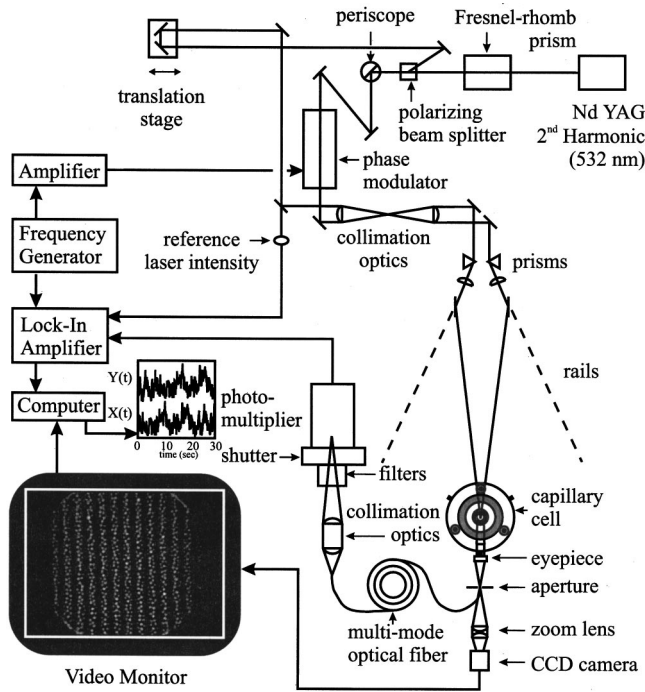(2.21)

FIG. 6. Schematic illustration of the Fourier imaging correlation spectroscopy (FICS) apparatus. See text for explanation.

Thus an analysis of the trajectories of the dynamical variables X and Y via Eq. (2.21) provide a direct route to the intermediate scattering function, which is a fundamental quantity of interest to the theoretical description of liquid state dynamics. The static structure function is simply the $\tau = 0$ limit of Eq. (2.21):

$$S(k) = \frac{4\tau_{LI}^2}{\kappa^2 I_0^2} \{\langle X^2 \rangle + \langle Y^2 \rangle\}. \tag{2.22}$$

III. EXPERIMENTAL SYSTEM

A. Instrumentation

In Fig. 6 we show a schematic of the FICS apparatus used in our studies. The instrument is designed to operate in either direct visualization or FICS mode. The sample chamber (a capillary cell used to prepare thin-film colloidal suspensions) is held at the sample plane of a fluorescence microscope, and placed at the focus of two intersecting laser beams. The excitation source is the continuous wave frequency doubled output of a Spectra Physics Nd:YAG (yttrium aluminum garnet) laser ($\lambda_{ex} = 532$ nm); its output power (measured just before sample incidence) is typically set below 0.1 mW to minimize photodegradation during data acquisition ($\sim$1 min). The laser beam is divided into two optical paths by a Fresnel-rhomb prism and a polarizing beam splitter. The transmitted S-polarization component of the beam is rotated 90° using a periscope to match the P polarization of the reflected beam. The transmitted beam is passed through an electro-optic phase modulator (Conoptics), and then focused onto the sample using a long focal length lens ($f = 40$ cm). The second beam is reflected by a corner cube mirror, which is mounted onto a translation stage, before it is directed through an identical lens to the sample chamber. The two

beams produce an intensity interference fringe pattern inside the sample, with adjustable spatial period d_G, as described by Eq. (2.10).

The modulated fluorescence signal $I_G(t)$ is collected using a fused silica oil-immersion objective (Leica, Plan Fluotar, $100\times$, Na$=1.3$) and eyepiece (Zeiss, $5\times$). The image depth-of-field is limited by placing an adjustable aperture ($\sim$50 μm) at the focal plane conjugate to the sample. The signal is coupled into a multimode optical fiber (3M). The emission from the transmitting end of the fiber is imaged onto a thermoelectrically cooled photomultiplier tube (PMT, Hamamatsu, R3896) operating in current mode after filtration by an interference band-pass filter (CVI Laser, central wavelength 605 nm, bandwidth 10 nm, transmission efficiency 90%) and an excitation barrier filter. The modulated signal output of the PMT is detected using a digital dual-phase lock-in amplifier (Stanford Research Systems) that is referenced to the signal wave form used to drive the phase modulator. A computer, which controls an analog-to-digital data acquisition board (National Instruments), separately records (i) the average background fluorescence intensity $\kappa I_0 \hat{C}(0)$, (ii) the complex components of the demodulated signal, $X(t)$ and $Y(t)$; and (iii) the laser excitation power.

In practice, the mean fluorescence intensity, after being corrected for drifts in laser power (less than ±1%), is used to normalize the demodulated signal, effectively removing the influence of photodegradation. The ability to detect this signal is determined by the signal-to-background ratio, S/B, defined by

$$\frac{S}{B} = \frac{\kappa I_0 \langle \hat{C}^2 \rangle^{1/2}}{\kappa I_0 \hat{C}(0)} = \frac{\{\langle X^2 \rangle + \langle Y^2 \rangle\}^{1/2}}{\kappa I_0 \hat{C}(0)} = \left[\frac{1}{2} V \hat{C}(0)\right]^{-1/2}, \tag{3.1}$$

where V is the excitation volume. In our experiments on dense colloid suspensions ($\rho^* = 0.52$)$V \cong 9400$ μm^3 and $\hat{C}(0) \cong 0.45$ particles/μm^3, so that $S/B \sim 0.02$. Typically, for each experiment, 32 000 data points are collected at an acquisition frequency of 512 Hz. Individual data sets are repeated $\sim$10 times, cross-checked for consistency, and averaged together. Under these conditions we found $S/B \sim 2$%. The extent of photodegradation over the duration of a 10-min test measurement represents less than 1% loss of the total fluorescence signal. To determine the effects of laser induced photodamage on our measurements we perform power-dependent studies. Laser excitation intensities up to 10 mW result in identical autocorrelation functions to those obtained using 0.1 mW. Thus, at the relatively low excitation powers used in these studies, photodamage does not affect our measurements of colloidal thin-film dynamics.

Time-correlation functions of the X and Y trajectories are computed by averaging over t_{max} time origins according to

$$\langle A(t)A(t+\tau) \rangle = \frac{1}{t_{max}} \sum_{t_0=1}^{t_{max}} A(t_0)A(t_0+\tau), \tag{3.2}$$

where $A = X, Y$. Averages of the resulting autocorrelation functions are constructed from at least ten individual data sets. The decay time of the autocorrelation function is a measure of the time required for a labeled particle to move the
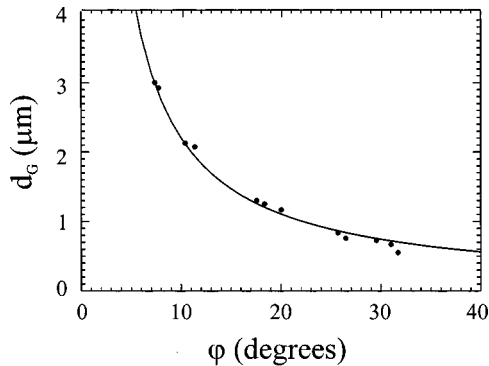
FIG. 7. Calibration curve showing the relationship between the fringe spacing d_G of the excitation grating and the angle of intersection φ between the two incident laser beams. Comparison is made between the values of d_G obtained from the measured intersection angles [calculated using Eq. (2.8), and shown as the solid line] and digital video analysis of grating images (filled circles) like that shown in the inset of Fig. 6.

distance k_G^{-1}. The upper limit to the temporal resolution of FICS measurements is determined by the modulation frequency. Essentially ten cycles of the reference oscillator are necessary to determine a single data point. For the experiments presented here, a modulation frequency of 50 kHz is used, corresponding to an instrument time resolution of 200 μsec.

When running in direct visualization mode, microscopic information is obtained by recording sequenced images of the sample plane via DVFM. This allows a direct comparison to be made between the time-correlation functions measured by the FICS method and the same quantities calculated from the microscopic particle trajectories via statistical mechanics [15,17,22]. Fluorescence images of the sample are collected using a charge-coupled device digital video camera (Cohu, Inc.). The frame speed of the CCD is adjustable; images are acquired at a rate ranging between 10 and 30 sec^{-1}. The shutter speed of the CCD is 1/100 of a second. The analog camera output is sent directly to the video port of a Silicon Graphics Indy (SGI) workstation. The SGI frame grabber supplied with the workstation is used to digitize 640×480 square pixel frames. A typical run consists of 1200 frames in sequence, corresponding to roughly 60 Mbyte of data. Image processing procedures are implemented using IDL (Research Systems, Inc.), a programming language optimized for visual data analysis. The pixel length is calibrated by imaging a transmission electron microscope (TEM) grid of known scale. The aspect ratio was determined to be 1 ± 0.1 and the calibrated pixel dimension was 1 pixel $= 0.1111 \pm 0.0015 \, \mu$m. The inset in Fig. 6 shows a fluorescence image of a typical particle configuration illuminated by a stationary excitation fringe pattern with $d_G = 4.0 \, \mu$m. To assess the accuracy of our pixel calibration, we compared DVFM measurements of the fringe spacing with the corresponding values obtained using Eq. (2.8). The results of these measurements are shown in Fig. 7. The two independent measurements of d_G are in excellent agreement, and we can therefore compare the FICS method's ability to probe density fluctuations of known spatial scale to known microscopic information.

B. Sample preparation

The system we have studied consists of 1-μm-diameter rhodamine labeled polystyrene particles confined between the closely spaced walls of an adjustable capillary cell (~ 1.5 μm). Because the particles surfaces are negatively charged, particle-particle interactions (and sample behavior) is strongly sensitive to counterion concentration and sample preparation conditions. For this reason, we employ a reproducible and consistent sample preparation protocol.

Colloid samples are obtained from Molecular Probes, Inc. as aqueous suspensions containing 2% solids. The particles are washed free of any surfactant impurities by dialysis (two days) followed by repeated sedimentation in purified water (Nanopure system, 18 MW, with a 0.2-μm filter). The particles are then resuspended in aqueous 20-μM sodium decyl sulfide (an ionic surfactant to stabilize the particles against aggregation) and 100-μM sodium azide (an antibiotic to prevent microorganisms from proliferating inside the sample chamber).

A schematic diagram of the capillary cell used in our experiments is shown in Figs. 8(A) and 8(B). A glass window (1/8-in. thickness) and No. 1 microscope cover slip (0.18-mm thickness) are held a fixed distance apart by spring-loaded stainless steel plates. The laser beams enter through an aperture in the top plate, while the fluorescence signal is collected by a microscope objective held beneath the bottom plate. The glass surfaces are cleaned by immersion in 1-M HCl followed by treatment with an octadecyl-silicone coating (Glassclad 18, United Chemical Technologies, Inc.). A small quantity of colloid suspension (~ 50–75 μL) is placed into the sample reservoir whose bottom is the glass coverslip. A narrow strip of closed-cell PVC foam (McMaster-Carr) serves as a compressible water-tight barrier, preventing solvent evaporation during the average lifetime of a sample (~ 5 days). The glass window is slowly lowered into the sample reservoir by retracting three kinematically mounted motorized micrometers (Picomotor, New Focus, Inc.). The micrometers are remotely and independently adjusted until the inner wall spacing between the glass window and coverslip reach ~ 1.5 μm. Samples are observed by running the instrument in visualization mode to determine if a monolayer suspension is formed. This is true when the particle centers clearly lie in a plane, and out-of-plane motion is suppressed.

The relative refractive index of the dielectric interface [used in Eq. (2.8)] for this thin-film geometry is an average that accounts for the octadecyl coating at the inner glass surface and the presence of the colloid suspension. This value for n($= 1.385$) was previously used to successfully describe evanescent wave dynamic light scattering studies performed on similarly prepared thin-film colloid systems [17].

IV. RESULTS AND DISCUSSION

In Fig. 9(A) we show a typical raw data set taken from FICS measurements performed on dilute monolayer suspensions ($\rho^* = 0.02$) of Rhodamine labeled colloidal spheres with $d_G = 1.0 \, \mu$m. At low density, the mean interparticle separation is large, $[L = (\rho^*/\sigma^2)^{-1/2} \sim 7.1 \, \mu$m], and the sys-
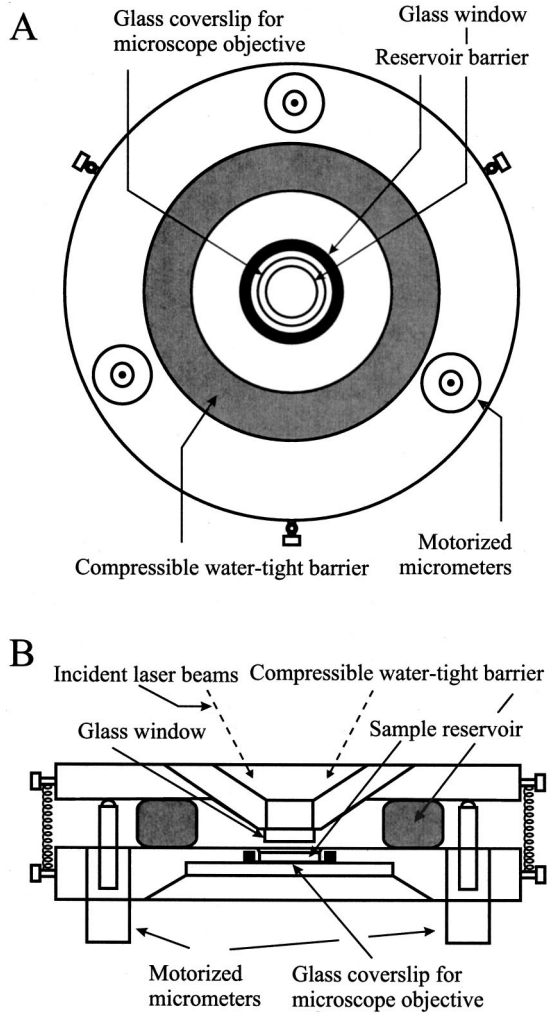
FIG. 8. Schematic diagram of the experimental capillary cell for thin-film colloidal suspensions. (A) Top view. (B) Side view. A glass window and a glass microscope coverslip are mounted to spring-loaded, parallel, stainless steel plates; their surfaces are held a fixed distance apart. Motorized micrometers are used to remotely control the inner wall spacing with submicron precision. A compressible water-tight barrier prevents solvent evaporation. Excitation beams enter through the top of the cell, while fluorescence and transmitted excitation is collected with a microscope objective (not shown) at the bottom.

tem behaves like a superposition of non-interacting Brownian particles for $d_G < L$. The signal trajectory shown consists of 2000 sequential points each separated by 2 msec. For the purpose of clarity, line segments connecting adjacent time points have been omitted. We observe that the phase angle α spans the entire range between zero and 2π. Furthermore, the static distribution is well fit to a two-dimensional symmetric Gaussian function of the X and Y coordinates. Table I lists the second moments of Gaussian fits to data corresponding to experiments performed at successively increasing fringe spacings. We note that the distributions are isotropic [i.e., $\langle X^2 \rangle \cong \langle Y^2 \rangle$] and that $S(k) \propto \langle X^2 \rangle + \langle Y^2 \rangle$, according to Eq. (2.22), is independent of the fringe spacing for $\sigma \lesssim d_G \lesssim L$. We can see that this is an expected result for a dilute suspension of particles if we consider the form for $S(k)$ written
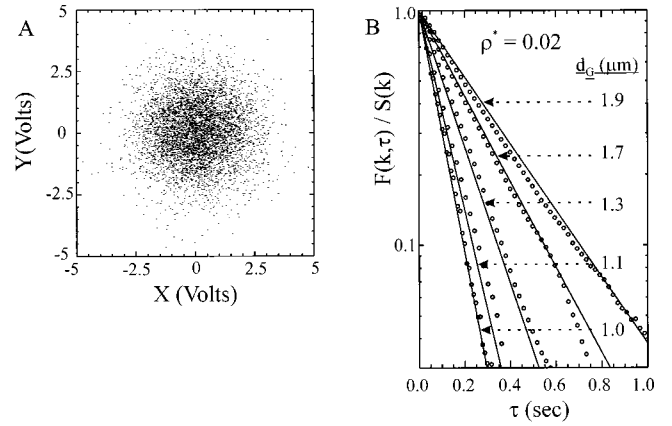

FIG. 9. (A) Demodulated fluorescence trajectory taken from a FICS measurement performed on a dilute monolayer suspension ($\rho^* = 0.02$) of rhodamine B labeled colloidal spheres ($\sigma = 1$ μm), with $d_G = 1.0$ μm. The phase shift $\theta = \theta_{ref} - \theta_G$ has been adjusted to $90°$, so that the X and Y components of the demodulated signal are proportional to the real and imaginary parts of $\hat{C}$, respectively. 2000 sequential points, each separated by 2 msec, are shown. Line segments connecting adjacent points have been omitted for clarity. The stationary distribution of points defines the probability $P[\hat{C}]$ from which spatial and temporal correlation functions are calculated [Eqs. (2.21) and (2.22)]. (B) The normalized intermediate scattering function, $F(k,\tau)/S(k)$, calculated from FICS measurements performed at five different fringe spacings corresponding to distances smaller than the average separation between neighboring particles ($L = 7.2$ μm). The data are single exponential in time and Gaussian in k. Solid lines are plots of Eq. (4.4) with $D_S = 0.3$ μm^2 sec^{-1}.

as an explicit function of particle positions that follows from substitution of Eqs. (2.1) and (2.2) into Eq. (2.3) [3]:

$$S(k) = N^{-1} \sum_i \sum_j \langle \exp[i\mathbf{k} \cdot (\mathbf{r}_i - \mathbf{r}_j)] \rangle. \qquad (4.1)$$

Since all of our measurements are in the microscopic high-k regime ($kL \gg 1$), the cross terms in Eq. (4.1) do not contribute to the overall sum leaving only the self-terms. This results in $S(k) = 1$ for a dilute suspension, in agreement with our observations.

In Fig. 9(B) we show calculations [according to Eq. (2.21)] of the intermediate scattering function constructed

TABLE I. Gaussian fit parameters for fluctuation measurements of $P[\hat{C}]$ for a dilute monolayer colloid suspension ($\rho^* = 0.02$). Amplitudes and inverse time constants of single-exponential fits to the corresponding normalized intermediate scattering functions [$F(k,\tau)/S(k) = A_0 \exp(-b_0\tau)$].

Fringe spacing, $d_G(\mu m)$	Wave number, $k_G(\mu m^{-1})$	$\langle X^2 \rangle$ (V)	$\langle Y^2 \rangle$ (V)	A_0	$b_0(\text{sec}^{-1})$
0.99	6.34	1.36	1.35	0.96	12.1
1.03	6.10	1.48	1.49	1.02	11.2
1.26	4.99	2.06	2.09	1.03	7.4
1.62	3.88	1.63	1.58	1.01	4.4
1.96	3.21	1.72	1.68	1.02	3.0

from five of the trajectory data sets listed in Table I. Under dilute conditions, the intermediate scattering function takes on a simplified form that can be understood if we substitute Eqs. (2.1) and (2.2) into Eq. (2.5), and write $F(k,\tau)$ as an explicit function of particles positions:

$$F(k,\tau) = N^{-1} \sum_i \sum_j \langle \exp\{i\mathbf{k} \cdot [\mathbf{r}_i(t) - \mathbf{r}_j(t+\tau)]\}\rangle. \tag{4.2}$$

For the same reason as explained in our treatment of Eq. (4.1), the condition $kL \gg 1$ implies that only the self-terms contribute to Eq. (4.2), which reduces to [2]

$$F_S(k,\tau) = \langle \exp\{i\mathbf{k} \cdot [\mathbf{r}(t) - \mathbf{r}(t+\tau)]\}\rangle. \tag{4.3}$$

In Eq. (4.3), $F_S(k,\tau)$ is the self-part of the intermediate scattering function. Equation (4.3) is further simplified by making use of the Gaussian model for single particle motion [2]. The Gaussian model makes use of the fact that the time scale associated with observation of the particle displacements is large compared to the relaxation time of the velocity autocorrelation function of the local particle positions. In this case, $[\mathbf{r}(t) - \mathbf{r}(t+\tau)]$ may be treated as a Gaussian random variable that leads Eq. (4.3) to take the following form for two dimensions:

$$F_S(k,\tau) = \exp[-k^2 D_s \tau], \tag{4.4}$$

where D_S is the self-diffusion coefficient. The data shown in Fig. 9(B) decay in time as a single exponential and with wave number as a Gaussian, in precise agreement with the theoretical prediction. The solid lines in Fig. 9(B) correspond to Eq. (4.4), with $D_S = 3 \times 10^{-9}$ cm^2 sec^{-1}. This value for the self-diffusion coefficient is in excellent agreement with that of the free diffusion coefficient, $D_0 = 0.707 k_B T/6\pi \eta a = 3.1 \times 10^{-9}$, calculated from the Stokes-Einstein equation with the necessary correction to account for the hydrodynamic friction due to the effect of the cell walls [23].

When measurements are performed on a dense system, the dynamics are complicated by multi-exponential decays that vary with k. Figure 10(A) displays a direct comparison of $F(k,\tau)/S(k)$ determined from FICS data (solid curves) and from DVFM data (circles) as a function of time for the same dense monolayer colloidal suspension ($\rho^* = 0.51$) previously described in Figs. 2, 3, and 4. FICS measurements were performed on this system at several different wave numbers, and are listed in Table II. In Fig. 10(A), decays are shown for three different wave numbers. The FICS data were constructed according to Eq. (2.21), while the microscopy data were calculated by Fourier inversion of the particle trajectories as described in Sec. II A. Agreement between the two independent measurements of the intermediate scattering function is excellent. For the highest value of k shown ($d_G = 0.86$ μm), the decay is nearly single exponential. As the wave number is decreased (or with decreasing fringe spacing) the decays begin to exhibit multiexponential character. This result is consistent with the interpretation that the $d_G = 0.86$ μm measurement is primarily sensitive to the "free" motion experienced by particles before they undergo colli-
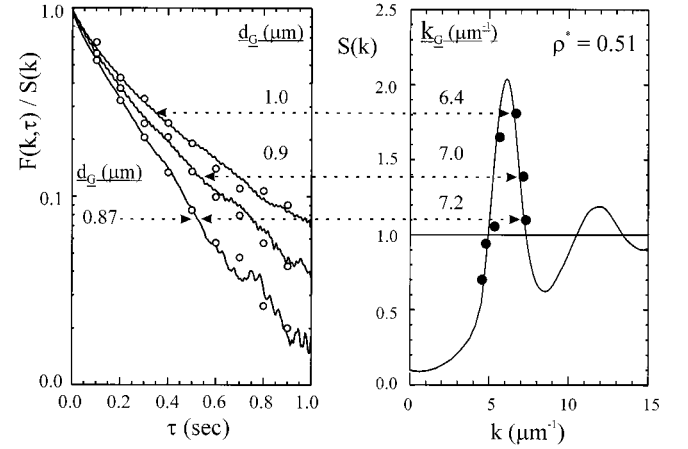

FIG. 10. Comparison between FICS and DVFM measurements performed on a dense monolayer suspension ($\rho^* = 0.51$). (A) The normalized intermediate scattering function $F(k,\tau)/S(k)$ is calculated according to Eq. (2.21) for the FICS data (solid curves). The DVFM data (open circles) are produced by Fourier inversion of particle trajectories as described in Sec. II A. (B) The static structure function $S(k)$ is calculated according to Eq. (2.22) for the FICS data (filled circles), while the DVFM data (solid curve) are calculated by Fourier inversion of the particle coordinates.

sions with their nearest neighbors, while the measurements corresponding to larger fringe spacings are sensitive to particle-particle interactions.

Figure 10(B) displays a direct comparison of $S(k)$ determined from FICS data (filled circles) and from DVFM data (solid curves) for the same dense sample described above. The FICS data were constructed according to Eq. (2.22), while the microscopy data were calculated by Fourier inversion of the particle positions according to Eq. (2.3). Agreement between the two independent measurements of the static structure factor is very good. The data points corresponding to the three time-dependent decays shown in Fig. 10(A) is also indicated. We note that the nonexponential and relatively slow relaxation at $k_G = 6.4$ μm^{-1} corresponds to a wave number near the first peak of $S(k)$. Our previous observations using video microscopy (Figs. 2–4) indicate that the relaxations for this system are highly complex and retarded near the peak of $S(k)$. The results shown in Fig. 10 demonstrate that our FICS measurements are equally sensitive to the dynamical and structural behavior of this dense quasi-two-dimensional fluid.

V. CONCLUSIONS

We have presented an experimental approach to study the structure and dynamics of fluorescently labeled complex fluids. Fourier imaging correlation spectroscopy (FICS) is based on the detection of modulated fluorescence signals, and measures temporal fluctuations of both the phase and amplitude of a spatial Fourier component of the particle number density. The phase and amplitude sensitivity of FICS arises from the sweeping of a patterned photo-excitation profile across the particle density at a much greater velocity than the speed at which an average particle can travel the interfringe spacing. The ability of the FICS method to directly probe both phase and amplitude of the complex Fourier com-

TABLE II. Gaussian fit parameters for fluctuation measurements of $P[\hat{C}]$ for a concentrated monolayer colloid suspension ($\rho^* = 0.52$). Amplitudes and inverse time constants of double-exponential fits to the corresponding normalized intermediate scattering functions $[F(k,\tau)/S(k) = A_0 \exp(-b_0\tau) + A_1 \exp(-b_1\tau)]$.

Fringe spacing, $d_G(\mu m)$	Wave number, k_G (μm^{-1})	$\langle X^2 \rangle$ (V)	$\langle Y^2 \rangle$ (V)	A_0	b_0 (sec^{-1})	A_1	b_1 (sec^{-1})
0.87	7.22	1.31	1.32	0.13	2.33	0.77	5.61
0.90	6.96	1.68	1.66	0.66	3.28	0.23	16.6
0.98	6.42	2.17	2.15	0.45	2.26	0.46	8.41
1.08	5.82	1.98	1.97	0.52	2.46	0.43	8.23
1.12	5.61	1.26	1.25	0.50	3.05	0.44	9.78
1.37	4.57	1.14	1.16	0.52	3.07	0.45	8.40
1.50	4.19	0.85	0.82	0.49	2.54	0.47	8.57

ponent is similar in spirit to dynamic light scattering (DLS) experiments in which heterodyne optical mixing techniques are employed to measure the scattered electric field-field correlation function [2]. Although we do not make use of the phase information obtained in the measurements presented here, FICS measurements performed simultaneously at many values of **k** yield, in principle, all of the necessary information to determine the time-dependent microscopic density. A clear advantage of the FICS method over light scattering is the promising application of an ultrasensitive phase-selective detection method to study systems that readily fluoresce under optical excitation. Thus, FICS is ideally suited to study systems under low-signal conditions. Although the most easily realized experiments are carried out at visible optical frequencies, analogous studies at much higher frequencies are possible. Furthermore, the FICS method may be extended to study excited state polarization, adsorption, Raman scattering, two-photon fluorescence, and four-wave mixing.

In comparison to direct visualization methods to acquire the same information, FICS experiments have both important advantages and limitations. While microscopy simultaneously records information on all spatial scales with a limited dynamic range, FICS measures spatial information at a single wave number at a time, and over a comparatively wide dynamic range ($10^{-8}-10^2$ sec). In essence, imaging experiments are many single-particle measurements carried out in parallel, while FICS experiments probe the time course of collective fluctuations from an N-body system. Because the length of a fluorescence trajectory from an N-body system is limited by photobleaching, the FICS method can access much longer time series by making more efficient use of the available photons emitted from the sample. Imaging experiments are capable of providing the real-space time-dependent density, $C(\mathbf{r},t)$. It is straightforward, although numerically intensive, to calculate the statistically meaningful time and space distribution functions from $C(\mathbf{r},t)$. We have focused on the van Hove correlation function $G(r,\tau)$ as a fundamental characterization of real-space distributions, and its Fourier transform—the intermediate scattering function $F(k,\tau)$—for reciprocal-space distributions. These same correlation functions are measured equally well using the FICS method, with its superior dynamic range.

In spite of the advantages of FICS to probe two-point spatial and temporal distributions of complex fluids, there remains an important limitation to this approach when com-

pared to direct visualization techniques. Microscopy experiments reveal information about the system corresponding to all spatial scales at one instant in time. In many dense complex fluids, there exist temporal and spatial regimes where the motions of neighboring particles are highly correlated. This gives rise to the so-called ''dynamic heterogeneity'' often observed in densely crowded systems such as polymer melts [24], colloid suspension [18], and supercooled fluids [25]. When experimentally probed on these intermediate time and length scales, the system appears to not satisfy the condition of ergodicity. That is, constituent particles exist in more than one local environment, or dynamical state, and the members of these separate populations do not readily interconvert. The superposition of dynamical behavior from these separate populations results in complex nonexponential relaxations of the time-correlation functions. As an example, we refer to Fig. 2(B), in which the dynamic heterogeneity of the system we have studied is apparent from the particle trajectory (see the discussion in Sec. II A). Since the ''hopping'' processes occur on the length scale of the nearest-neighbor spacing, the resulting nonexponential relaxation in the function $F(k,\tau)$ is most pronounced at the wave number k_{max}, corresponding to this spatial frequency (see Fig. 3). Nevertheless, it is not possible to infer the detailed dynamical picture conveyed by microscopy data from the functional form of $F(k,\tau)$ alone. Variations of the FICS approach, in which spatial information is simultaneously determined at more than one wave number at a time, should provide the necessary information to compute higher-order spatial and temporal distribution functions. Such information may easily identify the signatures of dynamic heterogeneity without the necessity of measuring the full spatial distribution at once.

The FICS method's ability to accurately characterize nonexponential relaxations of the intermediate scattering function is an important advantage over alternate fluorescence detection methods. The closest comparison can be made to fluorescence recovery after photobleaching (FRAP) where for the case of a patterned photoexcitation bleach pulse, an artificially imposed spatial heterogeneity is introduced into the system as an initial condition [10]. The relaxation of the bleached pattern is subsequently read out and analyzed assuming a diffusive transport model to determine the collective diffusion coefficient. FRAP experiments are powerful for the determination of transport coefficients; however, they are not capable of determining $F(k,\tau)$ and $S(k)$, since the

Fourier components corresponding to the natural length scales of the system are not directly measured. Thus, we expect the FICS approach to provide useful experimental information about the spatial and temporal scaling of dynamical properties for systems that have not been amenable to study by other methods.

Because of its low excitation power requirements, FICS is ideally suited for studying the dynamics of intracellular motion. We have recently applied FICS to study the details of mitochondrial translocation in live cells [15].

[1] P. M. Chaikin and T. C. Lubensky, *Principles of Condensed Matter Physics* (Cambridge University Press, Cambridge, 1995).

[2] B. J. Berne and R. Pecora, *Dynamic Light Scattering* (Krieger, Malabar, 1976).

[3] P. N. Pusey and R. J. A. Tough, in *Dynamic Light Scattering: Applications of Photon Correlation Spectroscopy*, edited by R. Pecora (Plenum, New York, 1985).

[4] There are a number of excellent articles that discuss this subject in the two volume series entitled *Liquids, Freezing and the Glass Transition, Les Houches 1989*, edited by J. P. Hansen, D. Levesque and J. Zinn-Justin (Elsevier, Amsterdam, 1989).

[5] S. Granick, Phys. Today **52** (7), 26 (1999).

[6] X. S. Xie and J. K. Trautman, Annu. Rev. Phys. Chem. **49**, 441 (1998).

[7] D. Magde, E. L. Elson, and W. W. Webb, Phys. Rev. Lett. **29**, 705 (1972); E. L. Elson and D. Magde, Biopolymers **13**, 1 (1974); D. Magde, E. L. Elson, and W. W. Webb, *ibid.* **13**, 29 (1974).

[8] For a review, see N. L. Thompson in *Topics in Fluorescence Spectroscopy, Vol. I: Techniques*, edited by J. R. Lakowicz (Plenum, New York, 1991), and references therein.

[9] Most commercial digital CCD cameras are limited to a maximum frame acquisition rate of ~30 Hz. Intensified cameras are capable of KHz acquisition frequencies, but require samples with high signal intensities.

[10] J. Davoust, P. F. Devaux, and L. Leger, EMBO J. **1**, 1233 (1982).

[11] R. L. Hanson, X. R. Zhu, and J. M. Harris, Anal. Chem. **70**, 1281 (1998).

[12] M. Hattori, H. Shimizu, and H. Yokoyama, Rev. Sci. Instrum. **67**, 4064 (1996).

[13] This point is often used to justify the central problems of equilibrium and nonequilibrium statistical mechanics. See for example, T. L. Hill, *Statistical Mechanics: Principles and Selected Applications* (Dover, New York, 1987), p. 2.

[14] J. P. Hansen and I. R. McDonald, *Theory of Simple Liquids* (Academic, London, 1986).

[15] D. Margineantu, R. A. Capaldi, and A. H. Marcus, Biophys. J. **79**, 1833 (2000).

[16] J. Crocker and D. G. Grier, J. Colloid Interface Sci. **179**, 298 (1996).

[17] A. H. Marcus, B. Lin, and S. A. Rice, Phys. Rev. E **53**, 1765 (1996).

[18] A. H. Marcus, J. Schofield, and S. A. Rice, Phys. Rev. E **60**, 5725 (1999); W. Kob, C. Donati, S. J. Plimpton, P. H. Poole, and S. C. Glotzer, Phys. Rev. Lett. **79**, 2827 (1997); C. Donati, J. F. Douglas, W. Kob, S. J. Plimpton, P. H. Poole, and S. C. Glotzer, *ibid.* **80**, 2338 (1998); E. R. Weeks, J. C. Crocker, A. C. Levitt, A. Schofield, and D. A. Weitz, Science **287**, 627 (2000); W. K. Kegel and A. von Blaaderen, *ibid.* **287**, 290 (2000); T. B. Schroder, S. Sastry, J. C. Dyre, and S. C. Glotzer, J. Chem. Phys. **112**, 9834 (2000); B. Doliwa and A. Heuer, Phys. Rev. E **61**, 6898 (2000).

[19] G. R. Fleming, *Chemical Applications of Ultrafast Spectroscopy* (Oxford University Press, New York, 1986).

[20] P. Horowitz and W. Hill, *The Art of Electronics* (Cambridge University Press, New York, 1986).

[21] K. V. Adair, P. Tekavec, and A. H. Marcus (unpublished).

[22] M. K. Knowles, T. J. Grassman, and A. H. Marcus, Phys. Rev. Lett. **85**, 2837 (2000).

[23] J. Happel and H. Brenner, *Low Reynold's Number Hydrodynamics* (Kluwer, Dordrecht, 1963).

[24] M. T. Cicerone and M. D. Ediger, J. Chem. Phys. **104**, 7210 (1996); **103**, 5684 (1995).

[25] M. D. Ediger, C. A. Angell, and S. R. Nagel, J. Phys. Chem. **100**, 13 200 (1996).